

## 1 **Supplementary Materials and Methods**

### 2 *Hippocampal slice preparation*

3 Experiments involving the use of animals were performed in accordance with guidelines provided  
4 by the Animal Protection Committee of Laval University. First, the animals were anesthetized with  
5 isoflurane. The brain was extracted and immersed in an oxygenated cutting ACSF solution  
6 maintained at 4 °C. The cutting ACSF solution contained (in mM): NaCl 87, NaHCO<sub>3</sub> 25, KCl  
7 2.5, NaH<sub>2</sub>PO<sub>4</sub> 1.25, MgCl<sub>2</sub> 7, CaCl<sub>2</sub> 0.5, glucose 25 and sucrose 75 (pH = 7.4, 330 mOsm). The  
8 brain was then dissected according to instructions for optimal preservation of the hippocampal  
9 mossy fibers (1). The brain hemispheres were glued on the specimen disk of a Leica VT1000S  
10 vibratome and submerged in cutting ACSF solution. Slices (300 μm) were cut and transferred to  
11 an oxygenated and heated (32 °C) ACSF solution containing (in mM): NaCl 124, NaHCO<sub>3</sub> 25,  
12 KCl 2.5, MgCl<sub>2</sub> 2.5, CaCl<sub>2</sub> 1.2 and glucose 10 (pH = 7.4, 300 mOsm). Slices were left to recover  
13 for 30 minutes at 32 °C. Slices were then left at room temperature. Experiments were started one  
14 hour after the slicing procedure.

15

### 16 *Whole-cell patch-clamp recording*

17 Hippocampal slices were maintained under a nylon mesh in a recording chamber under an upright  
18 microscope. Borosilicate glass electrodes had a resistance of 3 – 5 MΩ for CA3 pyramidal cell  
19 recordings. After obtaining a stable whole-cell configuration, CA3 pyramidal cells were held in  
20 voltage-clamp or in current-clamp. Voltage-clamp recordings were performed at -70 mV. Current-  
21 clamp recordings were performed at the resting membrane potential of the CA3 pyramidal cells (-  
22 70 ± 5 mV). Minimal stimulation of mossy fibers was performed using an electrode positioned in  
23 the stratum lucidum and connected to a constant current stimulus isolator (A360, WPI, Florida,  
24 USA). The pipette was gently moved in the stratum lucidum until large, fast and facilitating EPSCs  
25 could be recorded. The stimulation intensity was then decreased to achieve conditions in which  
26 both failures and successes could be observed. To confirm the mossy fiber identity of the recorded  
27 EPSCs or EPSPs, DCG-IV (1 μM) was applied in the end of a subset of experiments. Recordings  
28 in which the postsynaptic response was decreased by at least 80% were conserved for further  
29 analysis. Electrophysiological data was acquired with Molecular Devices equipment (Axopatch  
30 200B amplifier and Digidata 1322A, or MultiClamp 700B amplifier with Digidata 1440A) and the  
31 Clampex suite. The electrophysiological data was low-pass filtered at 2 kHz, digitized at 10 kHz

32 and recorded on a personal computer. For calcium imaging experiments, whole-cell patch-clamp  
33 recordings were obtained from granule cells with the solution described above, but lacking EGTA.  
34 This patch solution was supplemented with 40  $\mu\text{M}$  of the morphological dye Alexa-594 and 375  
35  $\mu\text{M}$  of the low-affinity calcium indicator Fluo-4FF. Granule cells were held in the current-clamp  
36 mode at their resting membrane potential. Action potentials were evoked by brief current injections  
37 (2 ms, 1 – 1.5 nA) in trains of 10 APs, at either 20 Hz or 100 Hz. Glass electrodes used for whole-  
38 cell recordings from granule cells had a resistance between 4 – 7  $\text{M}\Omega$ .

39

#### 40 *Random-access two-photon calcium imaging*

41 Following diffusion for at least 1 hour of the fluorophores in the granule cell, the axon was tracked  
42 to the CA3 region (2, 3). Giant MF boutons were unequivocally identified in the CA3 region based  
43 on their morphology imaged with the AlexaFluor-594 fluorescence. 20 sites evenly dispersed on  
44 the whole bouton were recorded quasi-simultaneously, yielding an imaging speed of 950 Hz. This  
45 recording paradigm allowed a good compromise between signal to noise ratio of the signal and the  
46 temporal resolutions, and therefore enabled recording calcium elevations generated by high-  
47 frequency firing of APs. The very low-affinity  $\text{Ca}^{2+}$  indicator Fluo-4FF proved critical to resolve  
48 high-frequency bursts of APs evoked at 100 Hz without indicator saturation. We used a custom  
49 built random-access two-photon microscope (2). Transmitted photons passed through a high-  
50 numerical aperture oil condenser ( $\text{NA} = 1.4$ ) and were low-pass filtered at 720 nm. Photons were  
51 separated by a dichroic mirror (580 nm) to independently collect red and green photons. Photons  
52 were then band-pass filtered at 500-560 nm for the green channel and 595-665 nm for the red  
53 channel. Both the red and the green photons were collected simultaneously. Collection of photons  
54 was performed using a pair of AsGaP photomultiplier tubes (H7422P-40, Hamamatsu) located  
55 close to the recording chamber. The laser and the acquisition system were controlled by a Labview  
56 custom-made software (4).

57

#### 58 *Analysis of electrophysiological and calcium imaging data*

59 Electrophysiological data were analyzed in Clampfit and in Igor Pro. AP probability was  
60 calculated from 20 sweeps. To avoid inducing long-term plasticity, sweeps were evoked every 30  
61 seconds. EPSC amplitude was measured from the average trace obtained from 20 sweeps. Calcium  
62 elevations recorded in giant MF terminals were exported to Excel database. The  $\Delta\text{G}/\text{G}$  ratio was

63 calculated for all trials and trials (50 – 140) were averaged together. The peak  $Ca^{2+}$  amplitude for  
 64 individual calcium transients was determined from baseline to peak. In all figures, symbols show  
 65 the mean and the error bars indicate the SEM.

66

67 *Non-stationary single compartment model of presynaptic  $Ca^{2+}$  dynamics*

68 The model is described by the following system of differential equations:

$$\frac{d[Ca^{2+}]}{dt} = j_{Ca} + k_{off}^I [CaI] - k_{on}^I [Ca^{2+}][I] + \sum_i (k_{off}^{B_i} [CaB_i] - k_{on}^{B_i} [Ca^{2+}][B_i]) - P_{rem}$$

$$\frac{d[I]}{dt} = k_{off}^I [CaI] - k_{on}^I [Ca^{2+}][I]$$

69 
$$\frac{d[B_i]}{dt} = k_{off}^{B_i} [CaB_i] - k_{on}^{B_i} [Ca^{2+}][B_i]$$

70 where the square brackets denote concentrations, and the superscript indices of the reaction rate  
 71 constants denote endogenous  $Ca^{2+}$  buffers  $B_i$  or the Fluo-4FF indicator  $I$ . The AP-dependent  
 72  $Ca^{2+}$  influx time course  $j_{Ca}$  was approximated by the Gaussian function

73 
$$j_{Ca} = \frac{\Delta[Ca^{2+}]_{total}}{\sigma\sqrt{2\pi}} \sum_i \exp\left(-\frac{(t-t_i^{AP})^2}{2\sigma^2}\right),$$
 where  $t_i^{AP}$  denotes the times of peaks of  $Ca^{2+}$  currents

74 during each action potential. The use of the low affinity  $Ca^{2+}$  indicator Fluo-4FF ( $K_d = 9.7 \mu M$ )

75 did not allow us to estimate resting  $[Ca^{2+}]_{rest}$  reliably, which in turn prevented the numerical

76 estimation of the total volume averaged presynaptic  $Ca^{2+}$  entry  $\Delta[Ca^{2+}]_{total}$ . Therefore we used

77 previous estimates for both  $[Ca^{2+}]_{rest} = 75 \text{ nM}$  and  $\Delta[Ca^{2+}]_{total} = 50 \mu M$  obtained with high affinity

78  $Ca^{2+}$  indicators (3, 5). Because in our experimental conditions  $[Ca^{2+}]_{ext} = 1.2 \text{ mM}$  (in comparison

79 to  $[Ca^{2+}]_{ext} = 2 \text{ mM}$  in ref. (3)) we reduced  $\Delta[Ca^{2+}]_{total}$  determined in ref. (3) by a factor of 1.5

80 based on the dependency of VGCC conductance on  $[Ca^{2+}]_{ext}$ .  $Ca^{2+}$  removal was approximated by

81 a first-order reaction  $P_{rem} = k_{rem} ([Ca^{2+}] - [Ca^{2+}]_{rest})$ . We assumed that a MFB terminal contains

82 three endogenous buffers ATP, CB and CaM. The complete set of model parameters and  $Ca^{2+}$

83 binding reactions, including concentrations and binding properties of the endogenous buffers,

84 which were previously determined using combination of electrophysiological, imaging and

85 immunocytochemical methods (6-9) is specified in **Supplementary Table 1**. The model was

86 numerically solved using the adaptive step-size Runge-Kutta algorithm. The model operated with  
87 only two adjustable (free) parameters: the unknown ratio between resting Fluo-4FF fluorescence  
88 signal and the background fluorescence and  $\text{Ca}^{2+}$  removal rate  $k_{rem}$ . Both parameters were  
89 constrained by a straightforward fitting procedure that would match the calculated and  
90 experimental fluorescence profiles.

91

### 92 *Spatial VCell model of MFB $\text{Ca}^{2+}$ dynamics*

93 A simulation unit, representing part of a MFB terminal with a single active zone (AZ), was  
94 modeled as a parallelepiped of size  $x = 0.5 \mu\text{m}$ ,  $y = 0.5 \mu\text{m}$  and  $z = 0.79 \mu\text{m}$ . The AZ was  
95 located in the XY base ( $z = 0.79 \mu\text{m}$ ) and contained a single rectangular VGCC cluster of  
96 dimensions  $40 \text{ nm} \times 80 \text{ nm}$  placed in the center of the AZ. The size of XY base corresponded to  
97 the average distance among different AZs in MFB terminals ( $0.5 \text{ mm}$ ) (10). The height of the  
98 simulation unit was adjusted to  $z = 0.79 \text{ mm}$  in order to match the magnitude of local VGCC-  
99 mediated  $\text{Ca}^{2+}$  influx at the AZ (see below) to the value of experimentally estimated  $\Delta[\text{Ca}^{2+}]_{total} =$   
100  $33.3 \mu\text{M}$ . We assumed that 28 VGCCs were evenly distributed within the VGCC cluster (11, 12).  
101 The average AP-evoked  $\text{Ca}^{2+}$  current was simulated using the five-state VGCC gating kinetic  
102 model in MFB (11) using the NEURON simulation environment (13, 14) and the experimentally  
103 determined MFB AP waveform (11), which was considered to be constant during burst of APs.  
104  $\text{Ca}^{2+}$  extrusion by the bouton surface pumps (excluding the AZ) was approximated by a first-order  
105 reaction  $j_{extr} = k_{extr} ([\text{Ca}^{2+}] - [\text{Ca}^{2+}]_{rest})$  (15, 16) located at the XY parallelepiped base opposite to  
106 the AZ;  $k_{extr}$  was calculated using the experimentally constrained single-compartment model  
107 average  $\text{Ca}^{2+}$  removal rate ( $k_{rem} = 400 \text{ s}^{-1}$ ) as  $k_{extr} = \frac{V}{S} k_{rem} = 320 \mu\text{m s}^{-1}$  (where  $V$  is the volume  
108 of the simulation unit and  $S$  is the area of the XY base). In the case of ‘Mobile CaM’ model we  
109 assumed  $[\text{CaM}]_{total} = 150 \mu\text{M}$  as was estimated in **Supplementary Fig. 10A**. In the case of ‘CaM  
110 dislocation’ model we assumed that all CaM molecules were located within a single  $10 \text{ nm}$  layer  
111 of VCell voxels adjacent to the AZ plasma membrane (i.e. at the  $0.5 \mu\text{m} \times 0.5 \mu\text{m}$  bottom base of  
112 the simulation unit). Concentration of CaM was 3 molecules /  $10 \text{ nm} \times 10 \text{ nm} \times 10 \text{ nm}$  voxel, as  
113 estimated in **Supplementary Fig. 10C**. The details of ‘CaM dislocation’ model are described in

114 our previous publication (14). Briefly, we assumed that upon binding of two  $\text{Ca}^{2+}$  ions by the C-  
115 lobe a CaM molecule can irreversibly dissociate from the plasma membrane ( $k_{off}^{CaM} = 650 \text{ s}^{-1}$ , ref.  
116 (14)) and freely diffuse in the cytosol.

117

118

119

120

121

122

123

124

125

126

127

128

129

130

131

132

133

134

135

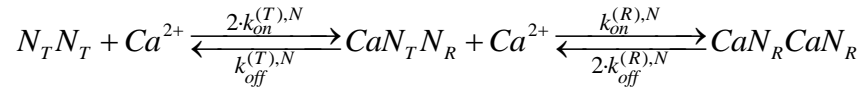
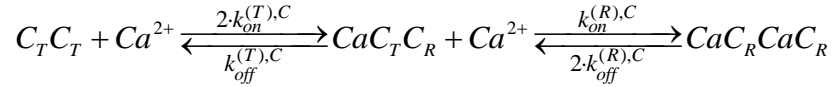
136

137 **Supplementary Table**

138 **Supplementary Table 1.**

139 **Properties of endogenous and exogenous Ca<sup>2+</sup> buffers used in non-stationary single**  
 140 **compartment and in multi-compartment VCell models of presynaptic MFB Ca<sup>2+</sup> dynamics.**

<b>Fluorescent Ca<sup>2+</sup> indicator Fluo-4FF</b>	
<u>Reaction:</u>	
$Fluo4FF + Ca^{2+} \xrightleftharpoons[k_{off}^{Fluo4FF}]{k_{on}^{Fluo4FF}} CaFluo4FF$	
<u>Reaction rates:</u>	
$k_{on}^{Fluo4FF}$	600 $\mu\text{M}^{-1} \text{s}^{-1}$
$k_{off}^{Fluo4FF}$	5,820 $\text{s}^{-1}$
$[Fluo4FF]_{total}$	375 $\mu\text{M}$
<b>ATP</b> (Supplementary refs. (7, 9, 14, 16, 17))	
<u>Reactions:</u>	
$ATP + Ca^{2+} \xrightleftharpoons[k_{off}^{ATP}]{k_{on}^{ATP}} CaATP$	
<u>Reaction rates:</u>	
$k_{on}^{ATP}$	500 $\mu\text{M}^{-1} \text{s}^{-1}$
$k_{off}^{ATP}$	1.0 x 10 <sup>5</sup> $\text{s}^{-1}$
$[ATP]_{total}$	0.9 mM (corresponding to 58 $\mu\text{M}$ $[ATP]_{free}$ at 1 mM $[Mg^{2+}]_{free}$ )
$D_{ATP}$	220 $\mu\text{m}^2 \text{s}^{-1}$
<b>Calbindin-D<sub>28K</sub></b> (Supplementary refs. (8, 18))	
<u>Reactions:</u>	
$CB_{fast} + Ca^{2+} \xrightleftharpoons[k_{off}^{CB_{fast}}]{k_{on}^{CB_{fast}}} CaCB_{fast}$	
$CB_{slow} + Ca^{2+} \xrightleftharpoons[k_{off}^{CB_{slow}}]{k_{on}^{CB_{slow}}} CaCB_{slow}$	
<u>Reaction rates:</u>	
$k_{on}^{CB_{fast}}$	87 $\mu\text{M}^{-1} \text{s}^{-1}$
$k_{off}^{CB_{fast}}$	35.8 $\text{s}^{-1}$
$[CB_{fast}]_{total}$	80 $\mu\text{M}$
$k_{on}^{CB_{slow}}$	11 $\mu\text{M}^{-1} \text{s}^{-1}$
$k_{off}^{CB_{slow}}$	2.6 $\text{s}^{-1}$
$[CB_{slow}]_{total}$	80 $\mu\text{M}$
$D_{CB}$	50 $\mu\text{m}^2 \text{s}^{-1}$
<b>Calmodulin</b> (Supplementary refs. (9, 14))	

Reactions:N-lobeC-lobeReaction rates for mobile CaM:N-lobe

$k_{on}^{(T),N}$	$770 \mu\text{M}^{-1} \text{s}^{-1}$
$k_{off}^{(T),N}$	$1.6 \times 10^5 \text{s}^{-1}$
$k_{on}^{(R),N}$	$3.2 \times 10^4 \mu\text{M}^{-1} \text{s}^{-1}$
$k_{off}^{(R),N}$	$2.2 \times 10^4 \text{s}^{-1}$

C-lobe

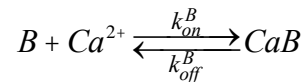
$k_{on}^{(T),C}$	$84 \mu\text{M}^{-1} \text{s}^{-1}$
$k_{off}^{(T),C}$	$2.6 \times 10^3 \text{s}^{-1}$
$k_{on}^{(R),C}$	$25 \mu\text{M}^{-1} \text{s}^{-1}$
$k_{off}^{(R),C}$	$6.5 \text{s}^{-1}$

$[CaM]_{total}$   $150 \mu\text{M}$  (mobile), 3 molecules / voxel (dislocation model)

$D_{CaM}$   $50 \mu\text{m}^2 \text{s}^{-1}$

In the case of CaM associated with membrane via interaction with neuromodulin we assumed that  $k_{off}^{(R),C}$  was increased 50-fold ( $k_{off}^{(R),C} = 325 \text{s}^{-1}$ ) (19, 20). We also assumed that upon  $Ca^{2+}$  binding by the C-lobe there was a 50% chance of CaM dissociation from neuromodulin (i.e.  $k_{off}^{CaM} = 2 \times k_{off}^{(R),C} = 650 \text{s}^{-1}$ , see ref. (14) for details.  $[CaM]_{total}$  was constrained in **Supplementary Fig. 10**.

**Fast high-affinity exogenous  $Ca^{2+}$  buffer mimicking behavior of endogenous MFB  $Ca^{2+}$  buffers**  
(Supplementary ref. (12))

Reaction:Reaction rates:

$k_{on}^B$	$800 \mu\text{M}^{-1} \text{s}^{-1}$
$k_{off}^B$	$176 \text{s}^{-1}$
$[B]_{total}$	$0.3 \text{mM}$
$D_B$	$50 \mu\text{m}^2 \text{s}^{-1}$

141

142

143

144 **Supplementary Figure Legends**

145 **Supplementary Figure 1 – MFBs count APs at any frequency and number**

146 (A) Representative voltage-clamp recordings of MFB evoked EPSCs in a CA3 cell. To explore  
147 whether AP counting occurs for any number of APs (in a physiological range), the number of  
148 stimuli in trains evoked at 20 Hz was varied between 1 and 10. The last stimulus was kept constant  
149 at 100 Hz. The amplitude of the last EPSC was measured. Gray traces show individual trials. Black  
150 traces show the average of 20 trials. (B) Normalized EPSC amplitude as a function of stimulus  
151 number for experiments illustrated in (A) ( $n = 25$  for 100 Hz;  $n = 7$  for each experiment with  
152 variable number of stimuli). Short-term facilitation was virtually identical for combined 20 Hz and  
153 100 Hz trains of stimuli described in (A), when compared to trains evoked purely at 100 Hz. (C)  
154 Trains consisting of 5 stimuli at 10, 20 or 100 Hz were followed by a single stimulus at a constant  
155 100 Hz to investigate if AP counting occurs at any frequency (in the physiological range of granule  
156 cell firing). Plotting the amplitude of the 6<sup>th</sup> EPSC as a function of prepulse frequency shows that  
157 the size of the 6<sup>th</sup> EPSC is independent of the prepulse frequency. Gray traces show individual  
158 neurons. The black trace is the average of  $n = 10$  cells.

159

160 **Supplementary Figure 2 – Post-tetanic potentiation changes the number of APs required to  
161 trigger CA3 pyramidal cell firing**

162 (A) Example traces of current-clamp recordings before and after the induction of PTP. Red arrows  
163 point to the first AP evoked by the stimulation trains. Insets show the expanded traces, focusing  
164 on the first 3 EPSPs. Note the truncated AP in the trace recorded following PTP. (B) Amplitude  
165 of the first EPSP in time. PTP was induced at  $t = 200$  s by a single train of 100 stimuli evoked at  
166 100 Hz ( $n = 6$ ). (C) Position of the first observed AP during the train as a function of time. In  
167 control condition, the first EPSP was generally observed at the 6<sup>th</sup> stimulus. PTP decreased the  
168 number of stimuli required to trigger CA3 pyramidal cell firing to 3, a value which gradually  
169 recovered to control value within 100 s ( $n = 6$ ).

170

171 **Supplementary Figure 3 – The rate of asynchronous release depends on the stimulation  
172 frequency**



173 (A) Voltage-clamp recordings showing the expanded portion of traces following 10 stimuli  
174 delivered at either 20 Hz (top) or at 100 Hz (bottom). Recordings shown are the overlay of 20  
175 consecutive traces. (B) Rate of asynchronous release as a function of stimulation frequency (20  
176 Hz: n = 6; 50 Hz: n = 8; 100 Hz: n = 8; 200 Hz: n = 3). For 100 Hz stimulation, the average  
177 frequency of asynchronous events was 5 Hz. This corresponds to ~ 0.05 quantal events during 10  
178 ms inter-spike interval. Considering that the average quantal size in our recordings was 50 pA, the  
179 asynchronous release will contribute only ~ 2.5 pA over a 10 ms window. On the other hand the  
180 amplitude of synchronous EPSCs recorded during 6AP trains was two orders of magnitude higher,  
181 ranging from ~ 125 pA (1<sup>st</sup> AP) to ~ 550 pA (6<sup>th</sup> AP).

182

183 **Supplementary Figure 4 – Amplitudes of individual AP-evoked presynaptic Ca<sup>2+</sup>-**  
184 **fluorescence transients are independent of spike number and burst frequency.**

185 Left, Representative image of a MFB labelled with AlexaFluor-594 with 20 recording sites for  
186 RAMP imaging shown with orange circles. An associated filopodia is visible to the right of the  
187 bouton. Middle, Corresponding Fluo-4FF experimental traces (black) in response to a 5X20 Hz +  
188 1X100 Hz AP burst (average of 181 sweeps). Red trace shows the non-stationary model fit. Right,  
189 Normalized peak amplitude of AP-evoked Fluo-4FF fluorescence as a function of AP number.  
190 Note that the amplitude of Ca<sup>2+</sup> fluorescence elevations remains constant during trains with  
191 variable frequency (n = 3).

192

193 **Supplementary Figure 5 – A single fast high-affinity buffer fails to replicate the experimental**  
194 **Ca<sup>2+</sup> imaging data.**

195 (A,B) Single compartment model-computed fluorescence traces during 10X20 Hz (A) and 10X100  
196 Hz (B) AP stimulation for the case of endogenous buffers (CB, CaM and ATP) or for the case of  
197 a single fast high-affinity exogenous buffer (Supplementary Table 1), which was shown to mimic  
198 the effect of the endogenous buffers on vesicular release in MFB terminals (12). (C,D) Normalized  
199 peak calcium transient amplitude as a function of AP number for experimental Fluo-4FF data  
200 (black trace), a model computed traces for 10X20 Hz (C) and 10X100 Hz (D) stimulation trains  
201 (n = 7 boutons for experimental data).

202

203 **Supplementary Figure 6 – Monte Carlo realization of AP-evoked response**

204 (A) Three representative Monte Carlo realizations of computed EPSCs in response to 6X100 Hz  
205 AP train in a MFB. Each trace is a sum of 125 individual Monte Carlo runs, corresponding to  
206 readily releasable pool size (RRP)  $m = 125$ . Insert, quantal response (this was used to compute  
207 EPSCs). (B) Individual realisations (gray traces, as shown in (A)) and average from 60 000  
208 individual realisations (black trace).

209

210 **Supplementary Figure 7 – Constraining the vesicle replenishment rate**

211 (A) Representative recording of CA3 pyramidal cell EPSCs during a 50X100 Hz train of stimuli  
212 used to evaluate the vesicle re-priming rate. (B) Responses to the first 10 stimuli and last 10 stimuli  
213 on (a) are shown enlarged. Light traces are individual trials. Black trace is the average of 7 trials.  
214 (C) Cumulative EPSC amplitude as a function of stimulus number. Modelling with various  
215 replenishment rates are shown in color. The experimental data (average of  $n = 9$  cells) was best  
216 fitted with a replenishment time  $\tau = 50$  ms, corresponding to the replenishment rate of  
217  $k_{rep} = 20$  s<sup>-1</sup>.

218

219 **Supplementary Figure 8 – Simulated MFB Ca<sup>2+</sup> dynamics and EPSCs during 5X100 + 1X20**  
220 **Hz and 6X20 Hz stimulation**

221 Comparison of  $[Ca^{2+}]$  dynamics during 5X100 Hz + 1X20 Hz stimulation (A) and 6X20 Hz  
222 stimulation (B). (C)  $[Ca^{2+}]_{residual}$  and  $[Ca^{2+}]_{amplitude}$  during the trains of APs shown in (A) and (B).  
223 Simulated EPSCs for 5X100 Hz + 1X20 Hz stimulation (D) and 6X20 Hz stimulation (E). Average  
224 of  $M = 60,000$  Monte Carlo runs for each paradigm scaled for RRP of size  $m = 125$ . (F) EPSC  
225 amplitude as a function of AP number for the simulations shown in (D) and (E).

226

227 **Supplementary Figure 9 – ‘Mobile CaM’ model, endogenous buffer dynamics during**  
228 **stimulation trains**

229 (A-C) Endogenous buffers dynamics during 5X20 Hz + 1X100 Hz (red) and 6X100 Hz (green).  
230 (D-F) Endogenous buffers dynamics during 5X100 Hz+ 1X20 Hz (blue) and 6X20 Hz (black) AP  
231 trains.

232

### 233 **Supplementary Figure 10 – Estimating CaM concentration in MFB terminals**

234 (A) The precise  $[CaM]_{total}$  in MFB is unknown. To estimate this value we computed the average  
235 release probability of individual readily releasable vesicles ( $p_v$ ) in response to a single AP for  
236 different  $[CaM]_{total}$  for the case of ‘Mobile CaM’ model. A previous study used dialysis of MFB  
237 terminals with fixed concentrations of BAPTA to demonstrate that the effect of MFB endogenous  
238 buffers on vesicular release can be approximated by a single fast high-affinity  $Ca^{2+}$  exogenous  
239 buffer (12). Therefore, as a reference point we used  $p_v$  value computed in our modelling  
240 framework for the case of such fast high-affinity buffer (see Supplementary Table 1). As a result  
241 we obtained an estimate for  $[CaM]_{total} = 150 \mu M$  which was within experimentally estimated range  
242 of neuronal  $[CaM]_{total}$  (9). (B) The steep dependency of  $p_v$  on  $[CaM]_{total}$  suggested a dominant  
243 effect of CaM N-lobe on  $[Ca^{2+}]$  transient at the release site. In agreement with this removal of CB  
244 or CaM C-lobe from the model resulted in only minor increase in AP-evoked  $[Ca^{2+}]_{peak}$  and  
245 simulated EPSC amplitude. In contrast removal of CaM N-lobe resulted in  $\sim 2.7$  fold increase of  
246  $[Ca^{2+}]_{peak}$  and  $\sim 9.5$  fold increase of EPSC amplitude. (C) Constraining  $[CaM]_{total}$  in the AZ in the  
247 limiting case of ‘CaM dislocation’ model. In this case we considered that at the beginning of VCell  
248 simulations all CaM molecules were located within a 10 nm layer of voxels located at the bottom  
249 plane of the modelling unit corresponding to the AZ (Fig. 4 A,F). Vesicular release probability  $p_v$   
250 was calculated for different number of CaM molecules in a 10 nm x 10 nm x 10 nm voxel and  
251 compared to the same reference point as in (A). As a result we obtained an estimate for the local  
252  $[CaM]$  in the AZ  $\sim 3$  molecules / voxel.

253

### 254 **Supplementary Figure 11 – Effect of CaM dislocation on active zone $Ca^{2+}$ dynamics and** 255 **vesicular release**

256 (A) Snapshots of spatial distribution of normalized total [CaM] (which accounts for all CaM  
257 molecules irrespective of their  $\text{Ca}^{2+}$  binding state) in the AZ plane, illustrating progressive  
258 dislocation of CaM from the membrane during AP stimulation predicted by ‘CaM dislocation  
259 model’ for 5X100 Hz + 1X20 Hz and 6X20 Hz stimulation patterns. (B) VCell-computed  $[\text{Ca}^{2+}]$   
260 transients at the release site during 5X100 Hz + 1X20 Hz and 6X20 Hz AP trains and (C)  
261 corresponding simulated EPSCs for the case of ‘CaM dislocation’ model. (D) Summary graph  
262 showing that experimentally observed short-term facilitation levels are likely to be explained by  
263 joint contribution of the two limiting cases represented by ‘Mobile CaM’ (low facilitation) and by  
264 ‘CaM dislocation’ (high facilitation) models that both allow AP counting logic.

265

### 266 **Supplementary Figure 12 – Vesicle occupancy of the release site during AP stimulation**

267 Vesicle occupancy as a function of time for 5X20 Hz + 1X100 Hz (red) and 6X100 Hz (green)  
268 and 5X100 + 1X20 Hz (blue) and 6X20 Hz (black) for both the ‘Mobile CaM’ and ‘CaM  
269 dislocation’ models. The vesicle occupancy is higher for lower stimulation frequency due to  
270 vesicle re-priming.

271

272

273

274

275

276

277

278

279

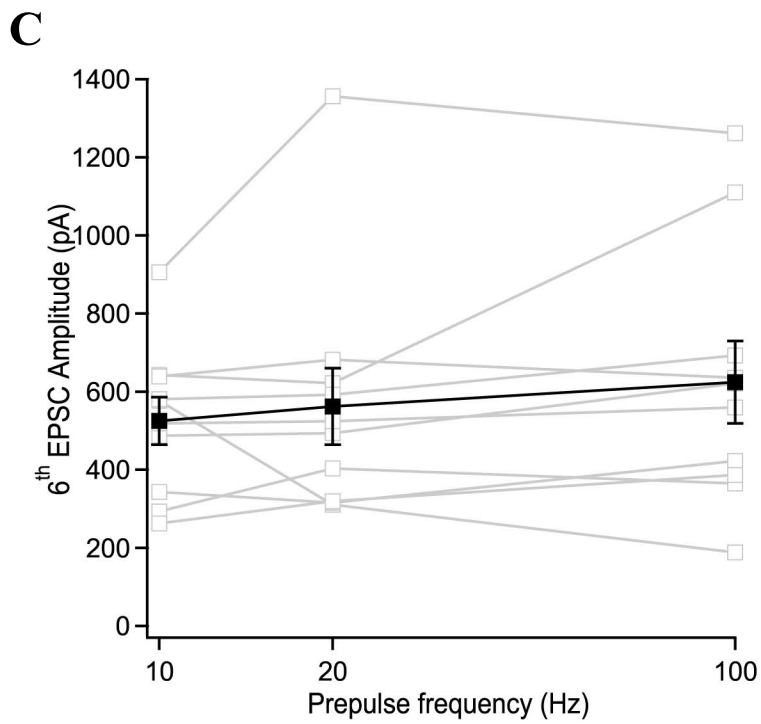
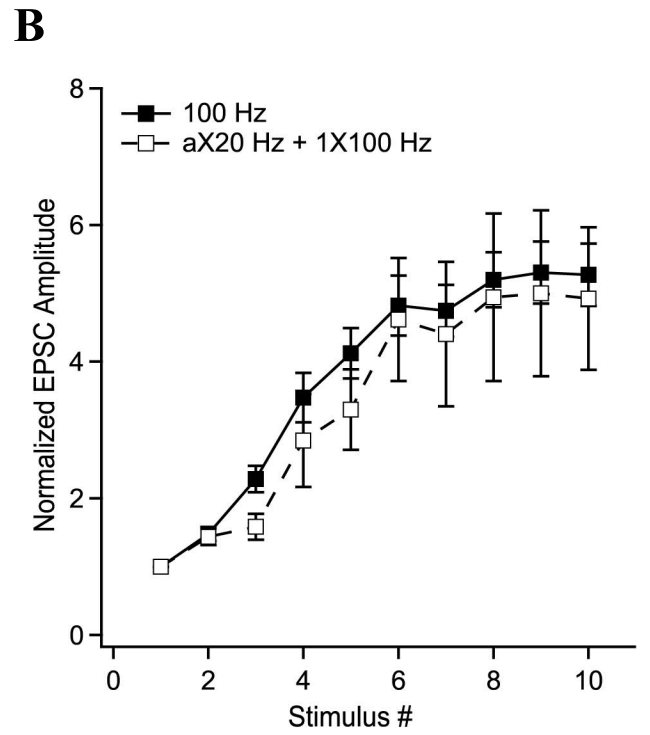
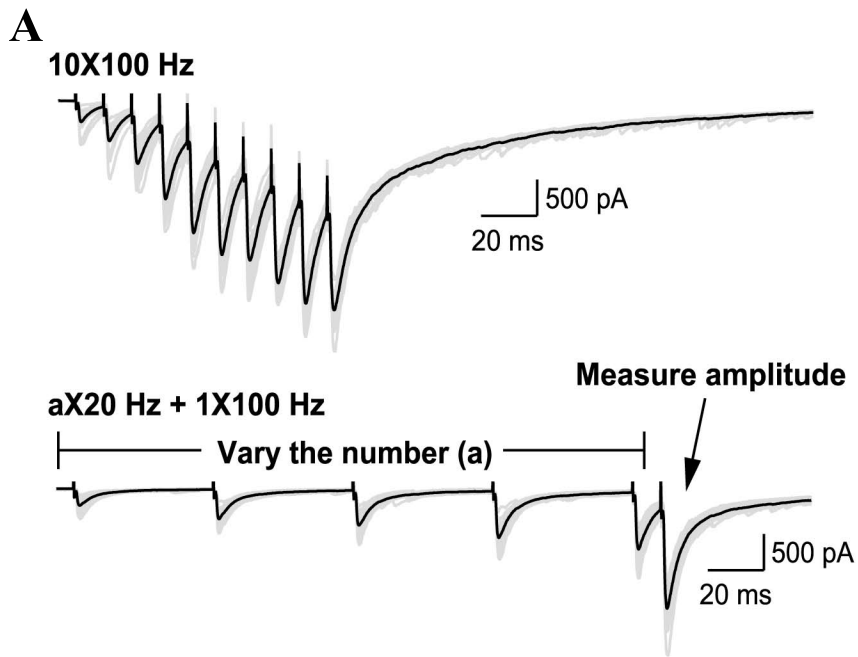
280

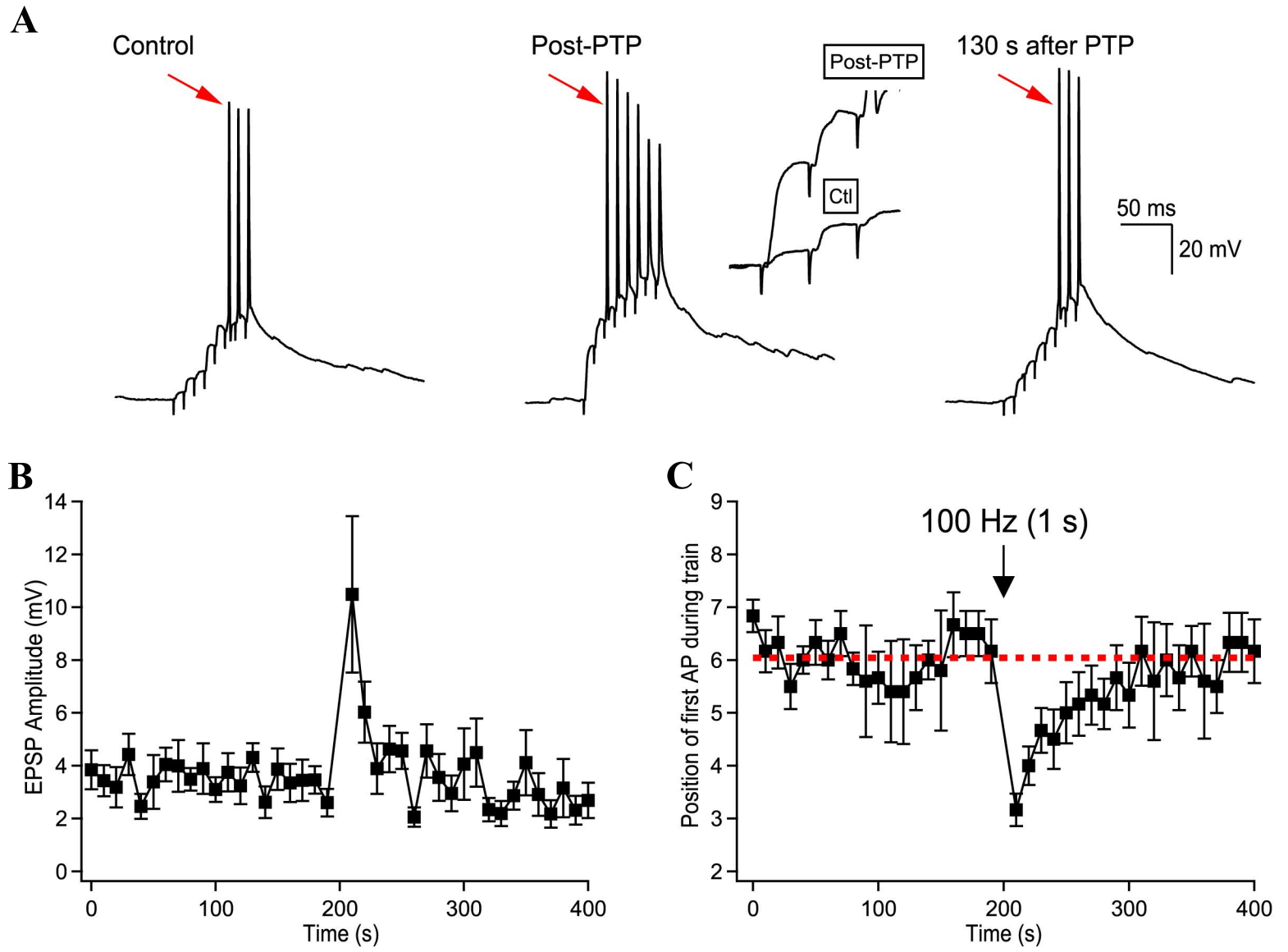
281

282 **Supplementary References**

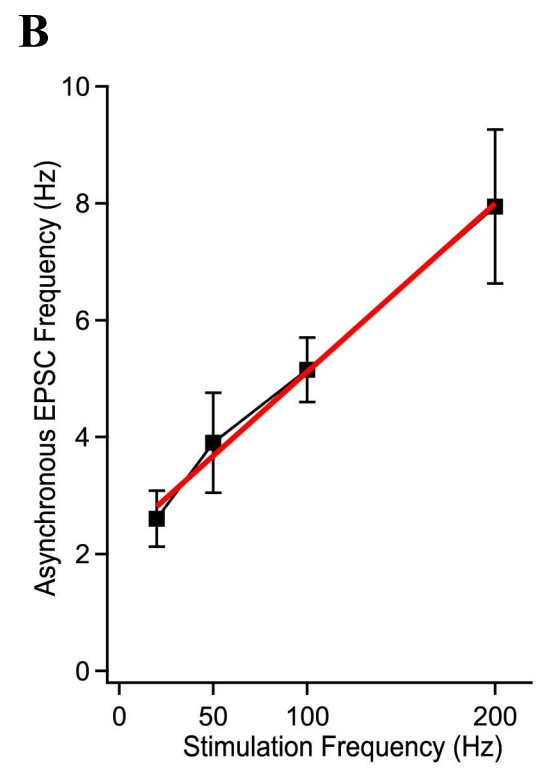
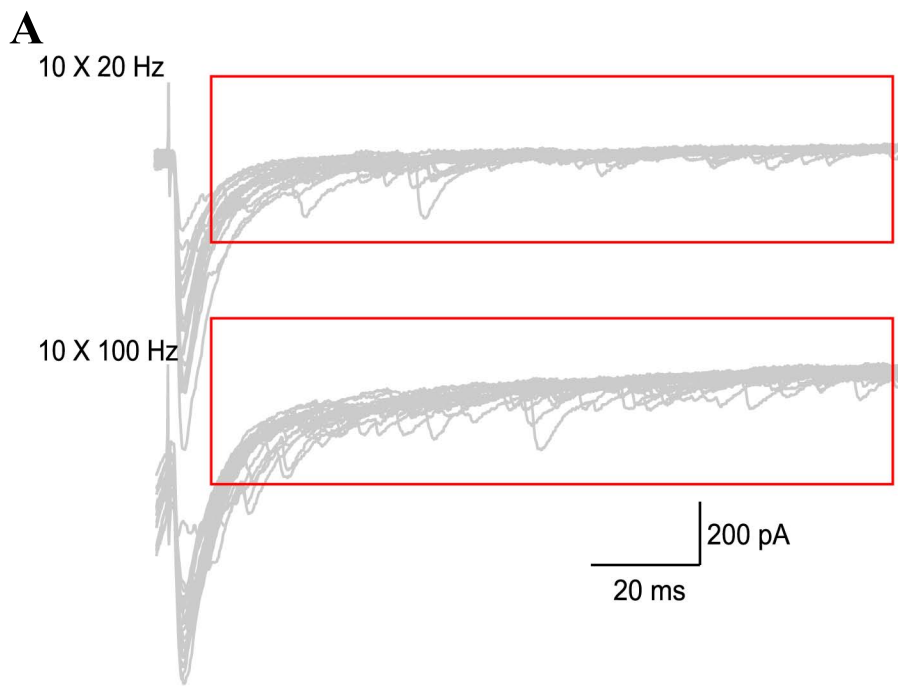
- 283 1. Bischofberger J, Engel D, Li L, Geiger JR, & Jonas P (2006) Patch-clamp recording from  
284 mossy fiber terminals in hippocampal slices. *Nature protocols* 1(4):2075-2081.
- 285 2. Chamberland S, Evstratova A, & Toth K (2014) Interplay between Synchronization of  
286 Multivesicular Release and Recruitment of Additional Release Sites Support Short-Term  
287 Facilitation at Hippocampal Mossy Fiber to CA3 Pyramidal Cells Synapses. *The Journal*  
288 *of neuroscience : the official journal of the Society for Neuroscience* 34(33):11032-  
289 11047.
- 290 3. Scott R & Rusakov DA (2006) Main determinants of presynaptic Ca<sup>2+</sup> dynamics at  
291 individual mossy fiber-CA3 pyramidal cell synapses. *The Journal of neuroscience : the*  
292 *official journal of the Society for Neuroscience* 26(26):7071-7081.
- 293 4. Otsu Y, *et al.* (2008) Optical monitoring of neuronal activity at high frame rate with a  
294 digital random-access multiphoton (RAMP) microscope. *Journal of neuroscience*  
295 *methods* 173(2):259-270.
- 296 5. Jackson MB & Redman SJ (2003) Calcium dynamics, buffering, and buffer saturation in  
297 the boutons of dentate granule-cell axons in the hilus. *The Journal of neuroscience : the*  
298 *official journal of the Society for Neuroscience* 23(5):1612-1621.
- 299 6. Muller A, *et al.* (2005) Endogenous Ca<sup>2+</sup> buffer concentration and Ca<sup>2+</sup> microdomains  
300 in hippocampal neurons. *The Journal of neuroscience : the official journal of the Society*  
301 *for Neuroscience* 25(3):558-565.
- 302 7. Meinrenken CJ, Borst JG, & Sakmann B (2002) Calcium secretion coupling at calyx of  
303 Held governed by nonuniform channel-vesicle topography. *The Journal of neuroscience :*  
304 *the official journal of the Society for Neuroscience* 22(5):1648-1667.
- 305 8. Nagerl UV, Novo D, Mody I, & Vergara JL (2000) Binding kinetics of calbindin-D(28k)  
306 determined by flash photolysis of caged Ca(2+). *Biophysical journal* 79(6):3009-3018.
- 307 9. Faas GC, Raghavachari S, Lisman JE, & Mody I (2011) Calmodulin as a direct detector  
308 of Ca<sup>2+</sup> signals. *Nature neuroscience* 14(3):301-304.
- 309 10. Rollenhagen A, *et al.* (2007) Structural determinants of transmission at large  
310 hippocampal mossy fiber synapses. *The Journal of neuroscience : the official journal of*  
311 *the Society for Neuroscience* 27(39):10434-10444.

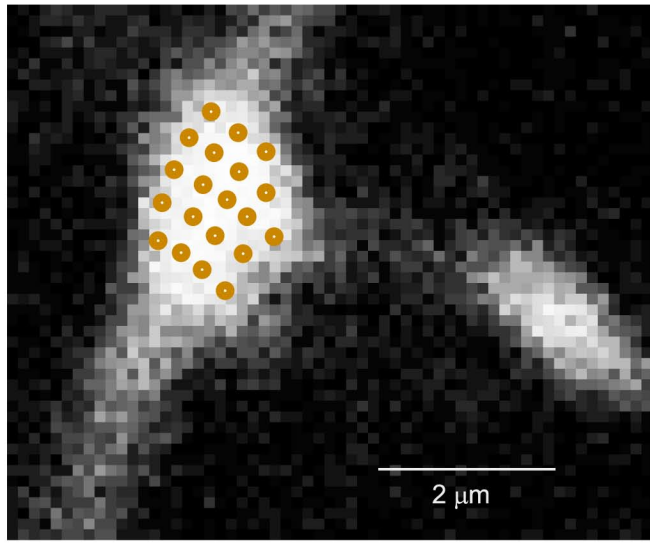
- 312 11. Bischofberger J, Geiger JR, & Jonas P (2002) Timing and efficacy of Ca<sup>2+</sup> channel  
313 activation in hippocampal mossy fiber boutons. *The Journal of neuroscience : the official*  
314 *journal of the Society for Neuroscience* 22(24):10593-10602.
- 315 12. Vyleta NP & Jonas P (2014) Loose coupling between Ca<sup>2+</sup> channels and release sensors  
316 at a plastic hippocampal synapse. *Science* 343(6171):665-670.
- 317 13. Hines ML & Carnevale NT (1997) The NEURON simulation environment. *Neural*  
318 *computation* 9(6):1179-1209.
- 319 14. Timofeeva Y & Volynski KE (2015) Calmodulin as a major calcium buffer shaping  
320 vesicular release and short-term synaptic plasticity: facilitation through buffer  
321 dislocation. *Frontiers in cellular neuroscience* 9:239.
- 322 15. Matveev V, Bertram R, & Sherman A (2006) Residual bound Ca<sup>2+</sup> can account for the  
323 effects of Ca<sup>2+</sup> buffers on synaptic facilitation. *Journal of neurophysiology* 96(6):3389-  
324 3397.
- 325 16. Ermolyuk YS, *et al.* (2013) Differential triggering of spontaneous glutamate release by  
326 P/Q-, N- and R-type Ca<sup>2+</sup> channels. *Nature neuroscience* 16(12):1754-1763.
- 327 17. Goswami SP, Bucurenciu I, & Jonas P (2012) Miniature IPSCs in hippocampal granule  
328 cells are triggered by voltage-gated Ca<sup>2+</sup> channels via microdomain coupling. *The*  
329 *Journal of neuroscience : the official journal of the Society for Neuroscience*  
330 32(41):14294-14304.
- 331 18. Eggermann E, Bucurenciu I, Goswami SP, & Jonas P (2012) Nanodomain coupling  
332 between Ca<sup>2+</sup> channels and sensors of exocytosis at fast mammalian synapses. *Nature*  
333 *reviews. Neuroscience* 13(1):7-21.
- 334 19. Gaertner TR, Putkey JA, & Waxham MN (2004) RC3/Neurogranin and  
335 Ca<sup>2+</sup>/calmodulin-dependent protein kinase II produce opposing effects on the affinity of  
336 calmodulin for calcium. *The Journal of biological chemistry* 279(38):39374-39382.
- 337 20. Hoffman L, Chandrasekar A, Wang X, Putkey JA, & Waxham MN (2014) Neurogranin  
338 alters the structure and calcium binding properties of calmodulin. *The Journal of*  
339 *biological chemistry* 289(21):14644-14655.



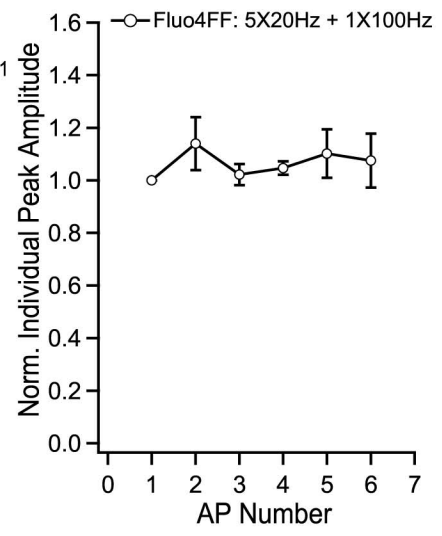
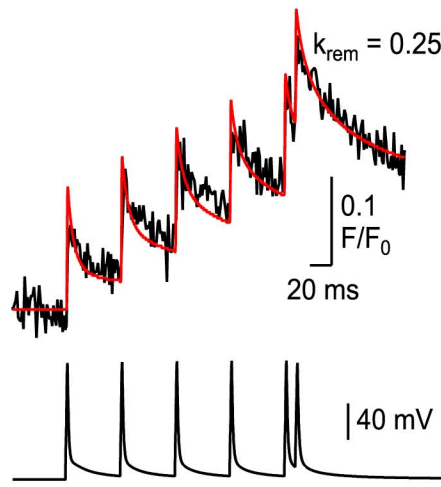


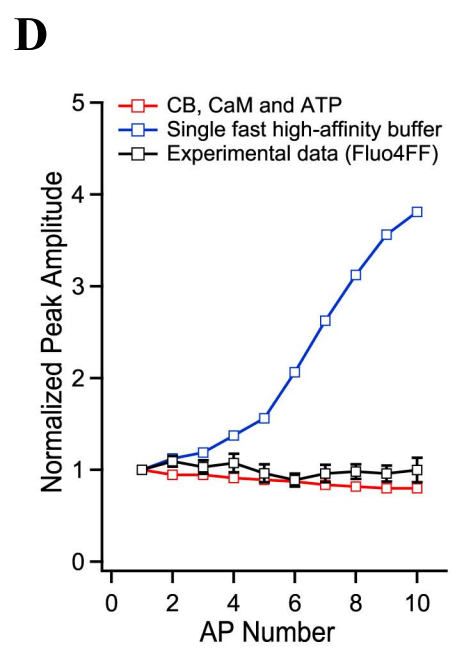
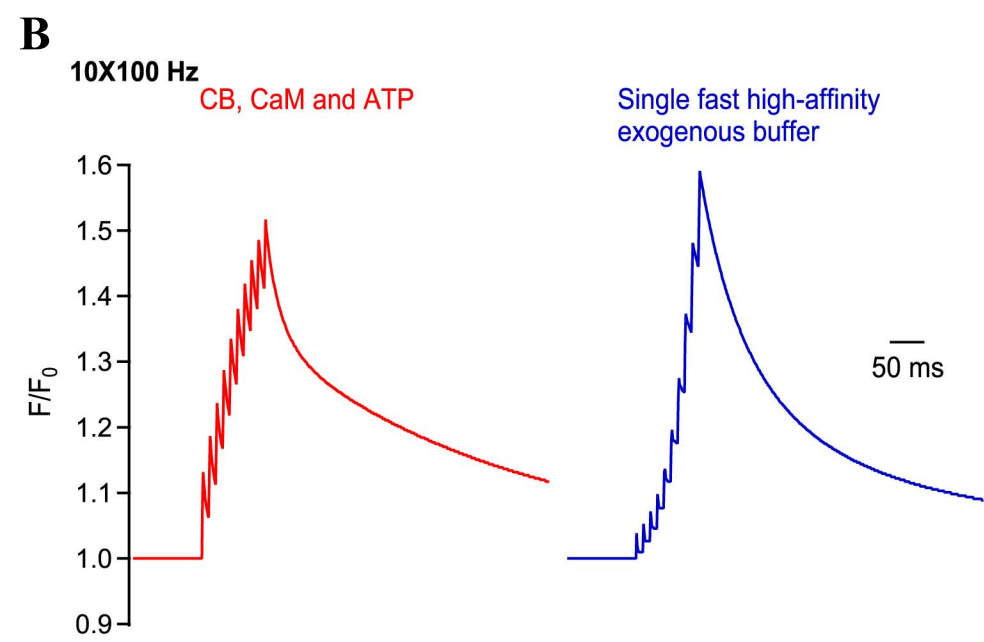
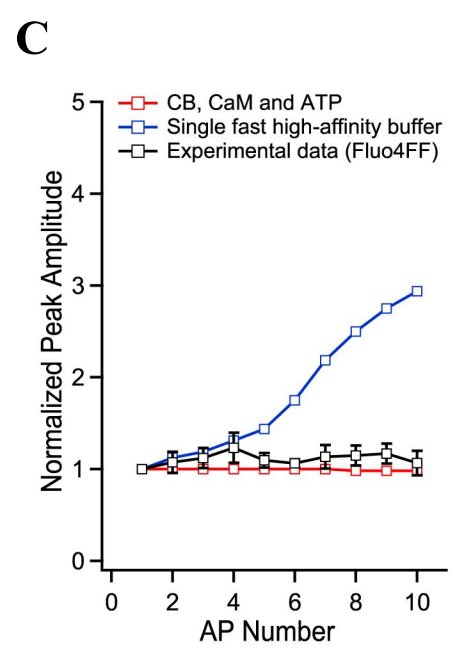
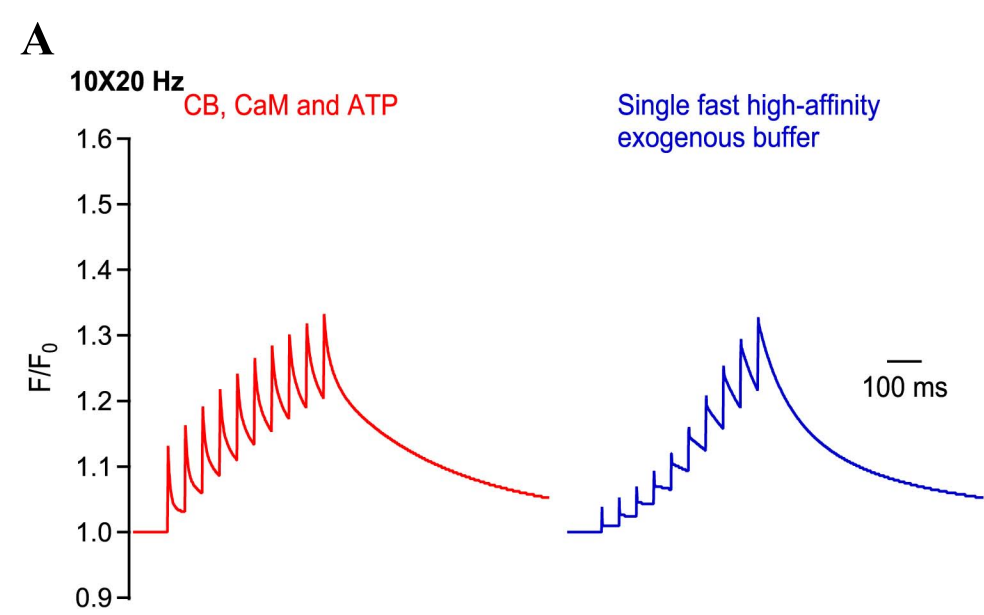




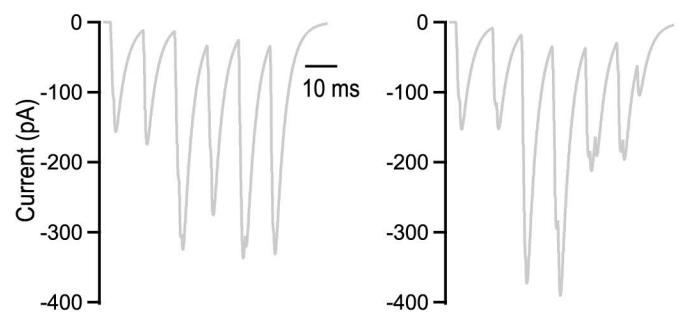
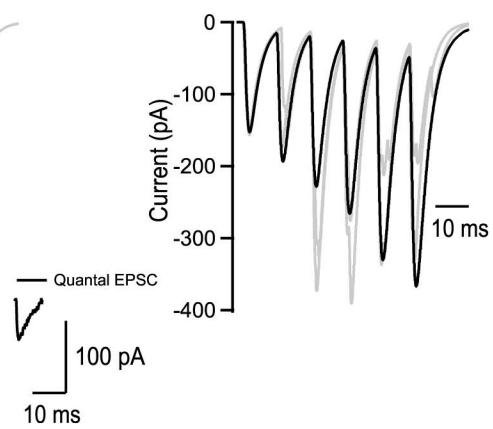


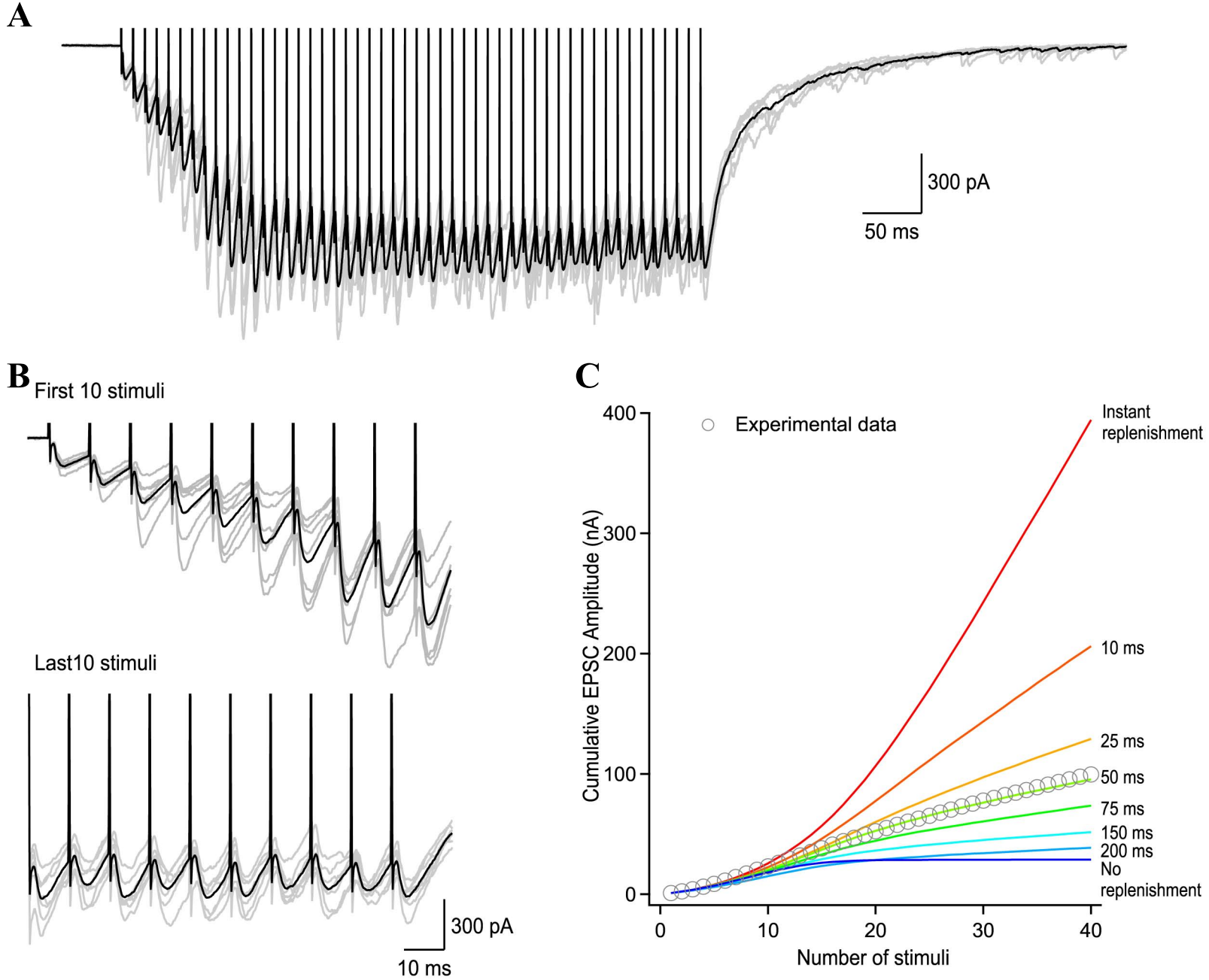
**5X20 Hz + 1X100 Hz**

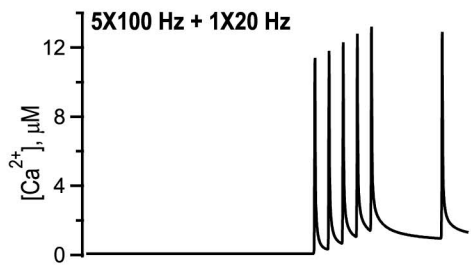
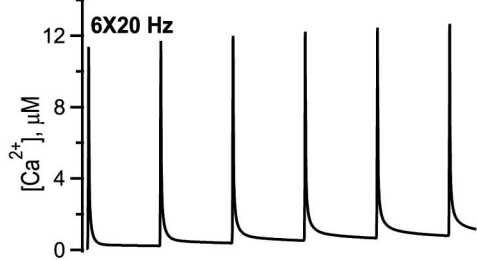
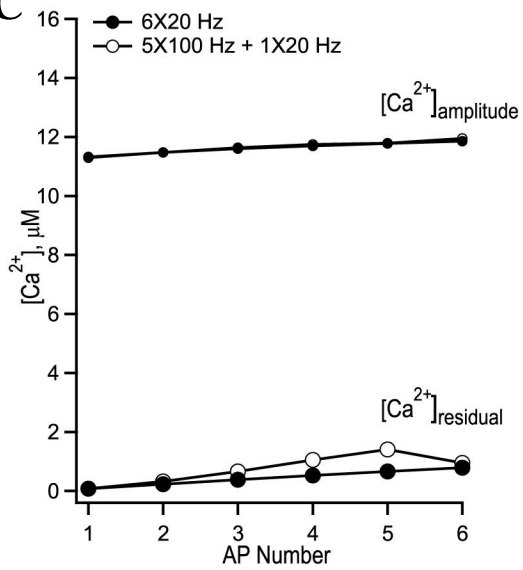
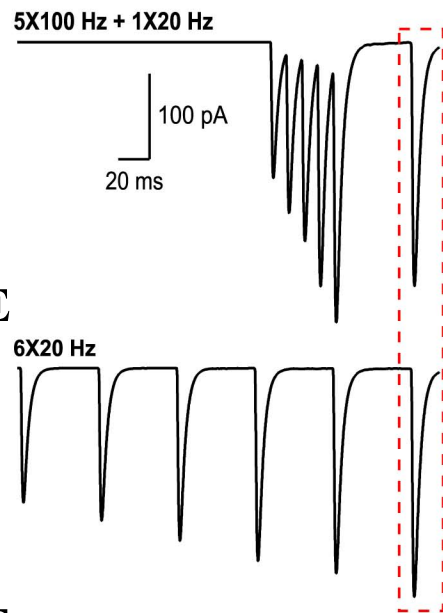
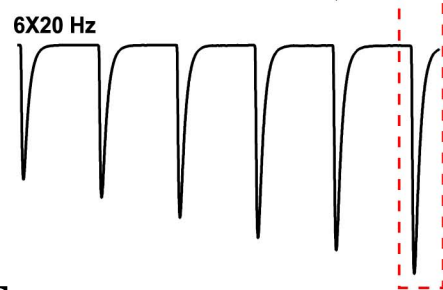
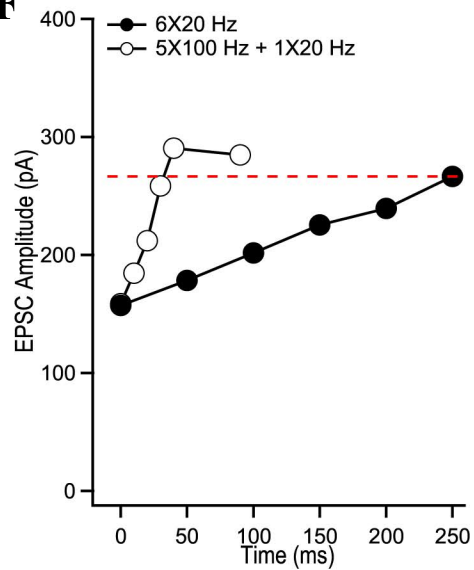


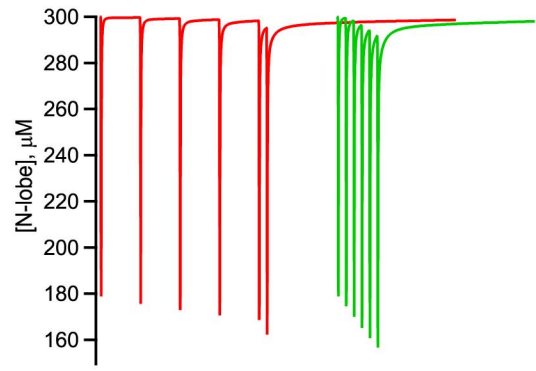
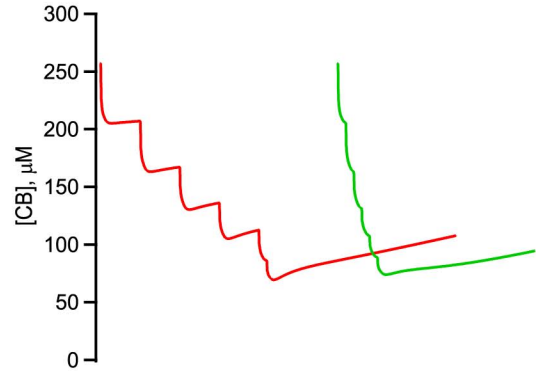
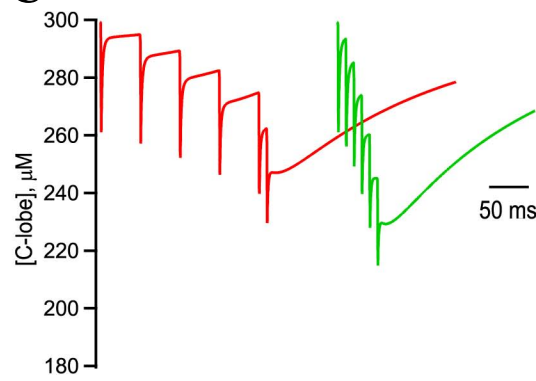
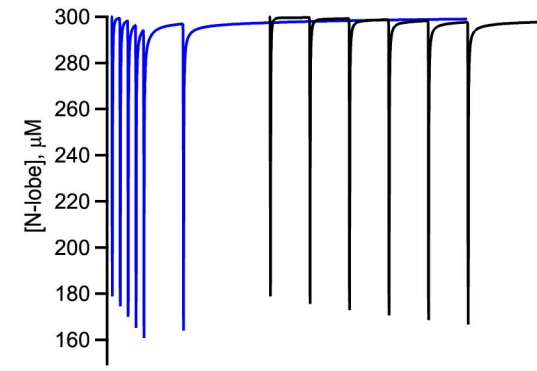
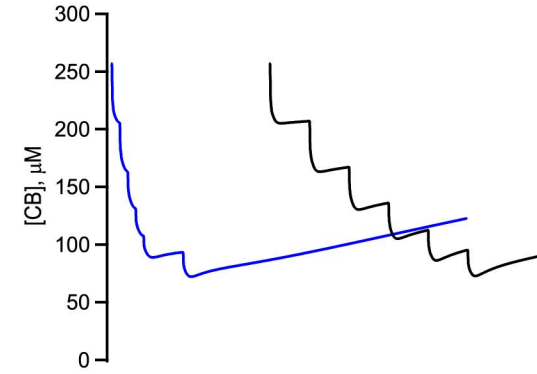
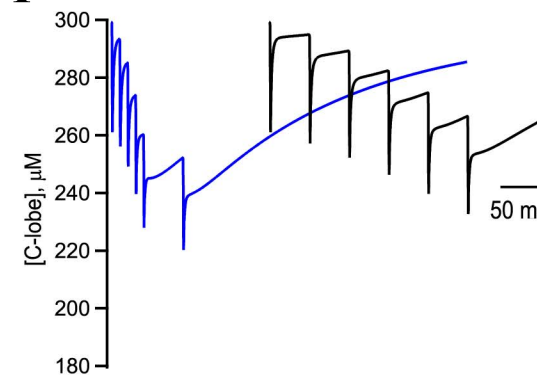


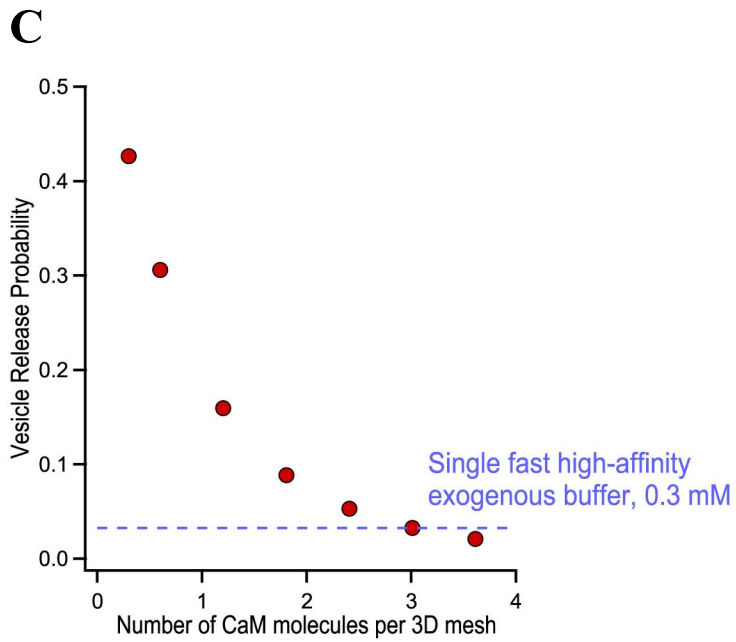
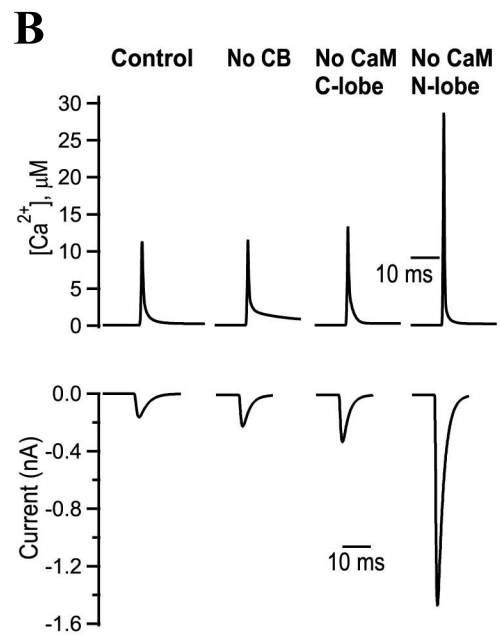
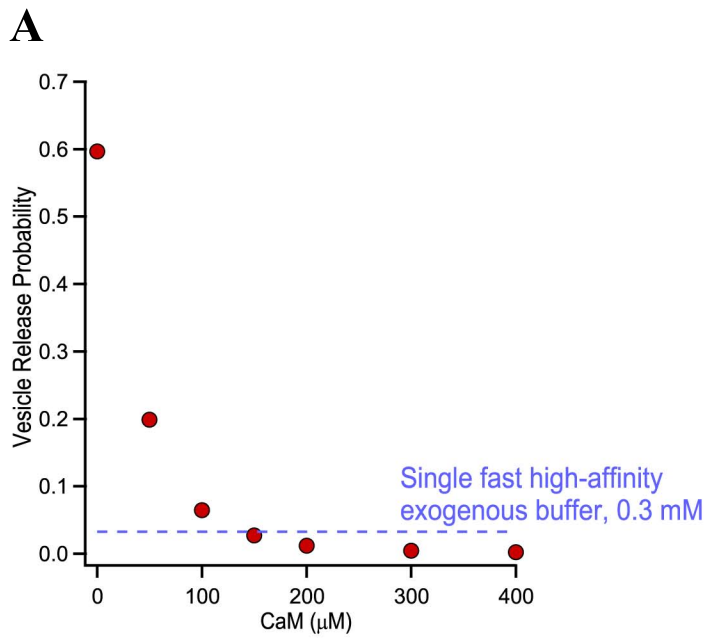
Supplementary Figure 5

**A****B**

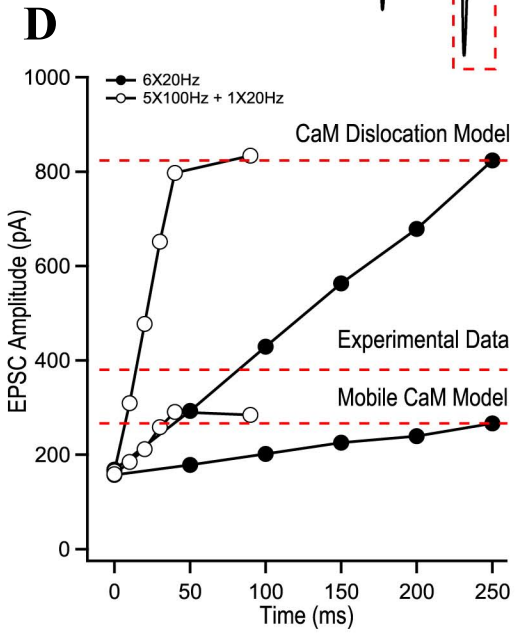
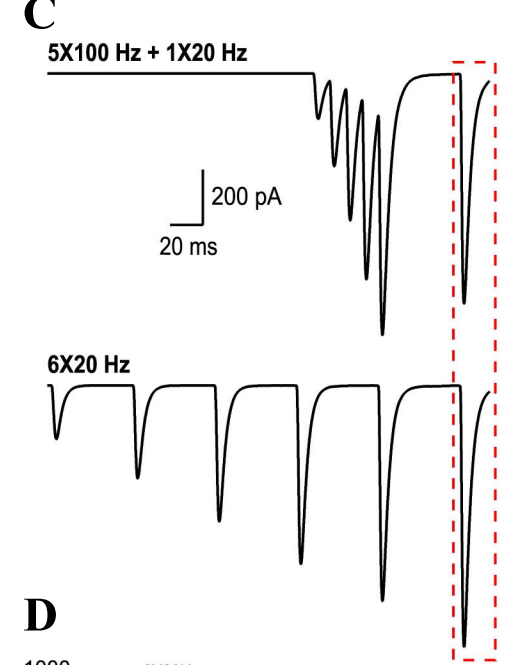
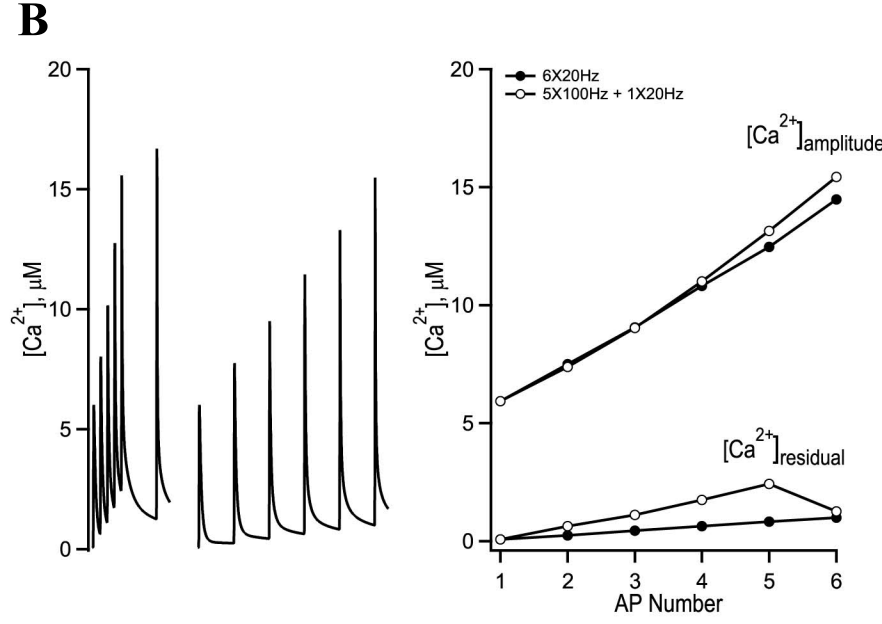
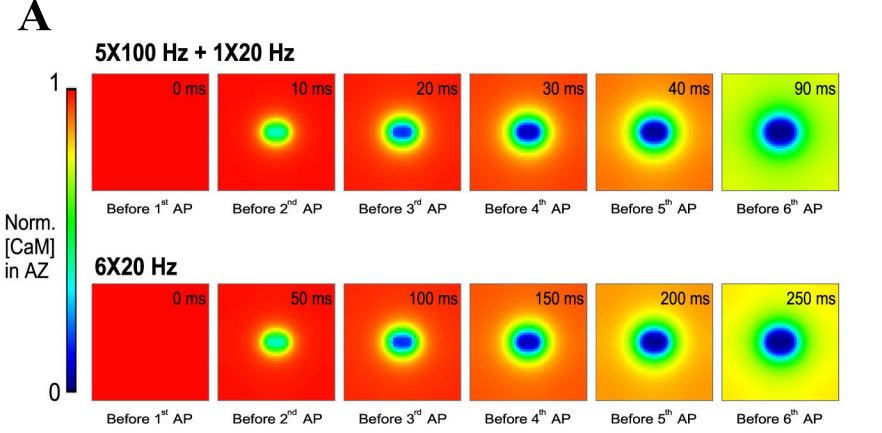


**A****B****C****D****E****F**

**A****5X20 Hz + 1X100 Hz and 6X100 Hz****B****C****D****5X100 Hz + 1X20 Hz and 6X20 Hz****E****F**

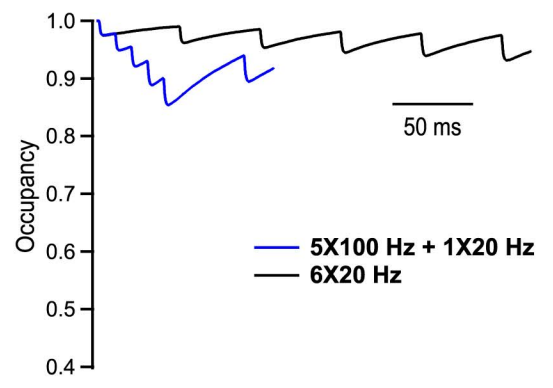
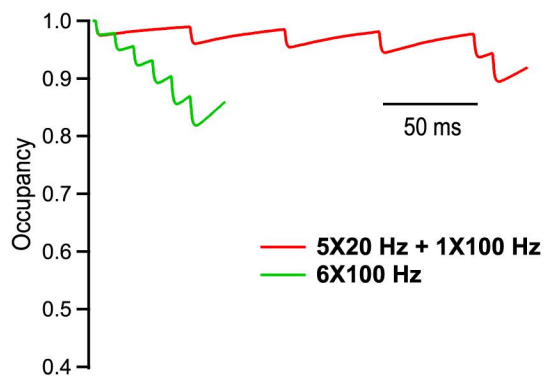






Supplementary Figure 11

**Mobile CaM**



**CaM Dislocation**

